Superconductor
Science and
Technology

PAPER • **OPEN ACCESS**

Quench dynamics in bare YBCO thin films with and without artificial pinning centers

To cite this article: S Mejia *et al* 2025 *Supercond. Sci. Technol.* **38** 105008

OPEN ACCESS
IOP Publishing
Superconductor Science and Technology
Supercond. Sci. Technol. **38** (2025) 105008 (8pp)
https://doi.org/10.1088/1361-6668/ae0dbe

Quench dynamics in bare YBCO thin films with and without artificial pinning centers

S Mejia[1,2,*], M M Aye[1], H Huhtinen[1] and P Paturi[1]

[1] Wihuri Physical Laboratory, Department of Physics and Astronomy, University of Turku, FI-20014 Turku, Finland
[2] University of Turku Graduate School (UTUGS), University of Turku, FI-20014 Turku, Finland

E-mail: samuel.m.mejia@utu.fi

Received 14 May 2025, revised 4 September 2025
Accepted for publication 30 September 2025
Published 10 October 2025

Abstract

In this study, we investigate the differences in the normal zone development between artificial pinning center free (APC-free) and $BaZrO_3$ (BZO)-doped $YBa_2Cu_3O_{6+x}$ (YBCO) thin films deposited on $SrTiO_3$ substrates. Normal zone propagation velocities (NZPV) and minimum quench energies (MQE) were measured over a wide range of temperatures (20–70 K) and magnetic fields (0–8 T) as a function of the percentage of the critical current ($\%I_c$). We found that lower MQE values are required in BZO-doped YBCO to trigger a quench. The most significant differences between APC-free and BZO-doped films in NZPV behavior were observed at high temperature and magnetic field values. Differences in quench characteristics can be attributed to variations in flux pinning mechanisms and current-carrying capabilities arising from the distinct properties of pinning centers. Through detailed analysis, this study enhances the understanding of how flux flow influences normal zone development in different YBCO thin films, providing insights relevant to technological challenges such as stability under high magnetic fields and quench detection in future high-temperature superconductor magnets.

Keywords: HTS superconductors, YBCO, BZO doping, quench, normal zone propagation velocity, minimum quench energy

1. Introduction

High-temperature superconductors (HTSs) are highly suited for applications requiring intense magnetic fields due to their high critical current densities, enabling efficient magnetic field generation with minimal energy loss through heat dissipation [1–5]. This makes HTS materials ideal for use in high-field applications, such as fusion reactors, particle accelerators, and advanced magnetic resonance imaging devices [6–8]. One of the most significant practical challenges in HTS magnet protection is developing a system that can quickly detect and respond to a transition from the superconducting to the normal state known as quench. Understanding key properties, such as the normal zone propagation velocity (NZPV), the minimum quench energy (MQE), and the material's response to external stimuli, is critical in designing these protective systems [9–12].

Present HTS coated conductor fabrication methods create inhomogeneities along the length of the tape creating variations in the critical current. The I_c variation in a tape can be even 20% around the average [11]. Some parts of the tape therefore carry a larger percentage of the critical current than originally designed. If the current exceeds the I_c, the superconductor reverts to the normal state and these resistive parts produce heat due to Ohmic heating. These resistive parts are

* Author to whom any correspondence should be addressed.

referred to as hot spots. The temperature difference at the edges of the hot spot creates diffusion of the heat. If the generated heat flux is greater than the diffusion of the heat, the hot spot starts to expand along the tape. During a quench the velocity of the expanding normal state is the NZPV. The minimum dissipated heat that causes a quench is referred to as MQE [13].

For low-temperature superconductor (LTS) magnets, voltage detection methods are used for detecting a quench. The reason for this is a very low enthalpy margin that results in a rapidly propagating normal zone [12]. However, in their HTS counterparts, due to the significantly larger operational margin, the normal zone propagates at a much slower velocity [12]. The typical NZPV values for HTS are 1–10 $\frac{\text{mm}}{\text{s}}$ and for LTS are 1–10 $\frac{\text{m}}{\text{s}}$ making the difference about two to three orders of magnitude [14]. For LTS even 10 μJ is sufficient to initiate a quench but in HTS MQE is on the order of 1 J [9, 14]. Because of these differences, different quench detectors have been suggested for HTS magnets such as fiber optic [15, 16], acoustic [17, 18], or superconducting [19, 20] quench detectors. It is self-evident that understanding the quench behavior of HTS is of utmost importance for their practical applications. Quench characteristics, such as NZPV and MQE, have been measured for different YBCO coated conductors in multiple different studies [9–11, 13, 21–23].

To ensure the safe operation of coated conductors the quench needs to propagate faster. Different coated conductor architectures have been studied to understand the relevant parameters controlling the NZPV. It has been found that having a thin stabilizer with high electrical resistance and low heat capacity increases the NZPV of a coated conductor [24]. Also by increasing the current transfer length (CTL) between the superconductor and the stabilizer results in a faster propagating normal zone. One notable way of modifying this CTL has been to implement so called current flow diverter (CFD) architecture. The basics of this architecture are to insert a highly resistive layer as part of the coated conductor geometry. This increases the CTL and gives a better spatial distribution of heat generation when the normal zone redistributes the current [25]. Different methods that have been implemented in order to create a CFD architecture include, for instance, using chemical etching and sputtering to modify the silver layer on top of the superconductive part [24], using diffusion reaction between evaporated indium and the silver layer to form a stable intermetallic compound that acts as the CFD layer [26], and using inkjet printing, oxygen annealing and sputtering to create silver patterns with high interfacial resistance on the superconducting surface [27]. All of these methods have been able to increase the NZPV values of HTS coated conductors to the same range that is observed with LTS.

In simple thin films, the current flows always in YBCO because there are no metallic layers that enable the current sharing effect in coated conductors [12, 13], making them ideal for studying the physics behind the quench. Increasing current first induces vortex motion, such as thermally activated flux flow (TAFF), which dissipates heat, before reaching the actual I_c [28, 29]. Differences in the transport current behavior result in propagation that is not similar to that of the coated conductors. It has been well studied that the introduction of non-superconducting linear defects that have a diameter of a vortex core and penetrate through the sample are very effective in pinning the vortices. $BaZrO_3$ (BZO) can be used to create these artificial pinning centers (APCs) that have considerably increased the in-field critical current ($J_c(B)$) of YBCO [30–34]. According to our knowledge, quench characteristics of APC-free YBCO thin films nor coated conductors have been compared to their counterparts that include APCs.

In this work, we have studied differences in the quench characteristics for APC-free YBCO and BZO-doped YBCO thin films in wide temperature and magnetic field ranges. The largest differences in NZPV behavior were observed in high magnetic fields and high temperatures. We also observed that MQE values were lower for the BZO-doped sample. These differences in NZPV and MQE between the APC-free and BZO-doped YBCO films are discussed with the theory of flux pinning, which gives the opportunity to develop better superconductor tapes for future applications.

2. Experimental details

2.1. Methods

APC-free and BZO-doped YBCO thin films with thickness of ≈200 nm were prepared by pulsed laser deposition (PLD) on 10 mm × 10 mm $SrTiO_3$ (STO) (100) substrates. Both targets used in this work were prepared using the solid-state reaction method [35]. The BZO weight percentage of the BZO-doped YBCO target was 4 wt.%. This doping ratio is based on our previous work [30]. All critical PLD parameters required for successful film deposition are from our earlier optimizations [36].

Thin films were patterned into 50 μm-wide microbridges using maskless photolithography combined with wet chemical etching. This pattern is presented in figure 1. The procedure involved spin-coating Megaposit™ SPR™ 220–4.5 photoresist at 8000 rpm, followed by laser-writer exposure using a Dilase 250 system (Kloé). Development was carried out in a sodium hydroxide (NaOH) solution, after which the films were etched in a phosphoric acid (H_3PO_4) bath. The residual photoresist was subsequently removed with acetone.

Magnetic hysteresis loops of the samples were measured at 10 K using the quantum design physical property measurement system (PPMS) before the patterning process. From these loops the critical current densities of the samples were determined using the Bean model for a rectangular shape film $J_c = 2\Delta m/[a(1 - a/3b)V]$, where Δm is the opening of the hysteresis loop, a and b are the width and length of the film, and V is the volume of the film [37]. PPMS AC transport measurement system was used to measure the $I - V$ curves. Cs-corrected JEOL JEM 2200-FS scanning transmission electron microscopy using operation voltage of 200 kV with a high-angle angular dark-field detector was used to show the BZO nanorods in the BZO-doped sample. The NZPVs and minimum quench energies of the thin films were measured with PPMS that had National Instruments PXIe-1073 connected to it. PPMS was used to control the temperature and magnetic field of the system, and it also applied currents to the sample.

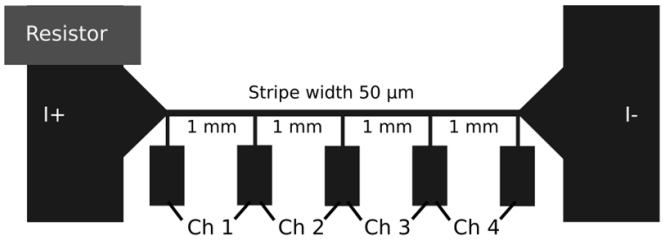

Figure 1. Schematic image of the YBCO microbridge used in this work. The thickness of the stripe is ≈200 nm. The dimensions of the resistor are 2.0 mm × 1.2 mm and the dimensions of the current and voltage contacts are 1.1 mm × 2.5 mm and 0.4 mm × 0.7 mm, respectively. In addition, the glued resistor is added to the right upper corner of the current contact pad which is the location where the heat pulse originates.

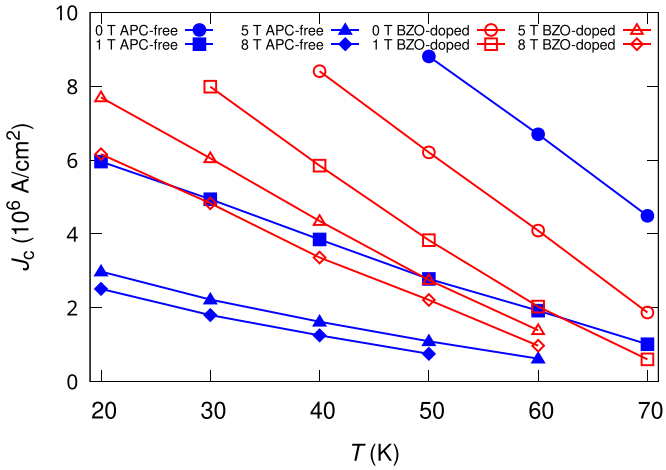

Figure 2. Critical current values for APC-free and BZO-doped YBCO samples measured at various temperatures and magnetic fields. The blue curves correspond to the APC-free sample and the red curves to the BZO-doped sample. Different symbols correspond to different magnetic field values. Note that the PPMS magnetometer's maximum current of 1 A (10 MA cm^{-2}) restricts measurement capabilities, particularly at low temperatures and in small magnetic fields.

NI PXIe-1073 was used to record the time evolution of the voltages within the sample. The quench measurement system was controlled using a LabVIEW platform.

2.2. Measurement procedure

The connections to the samples were made by wire bonding 33 μm Al-wire between the sample and the PPMS sample puck using TPT HB05 Wire Bonder. The current wires were at the ends of the microbridge and the voltage measurements were taken from the middle of the microbridge, as presented in figure 1. Two wires were bonded to a 220 Ω resistor that was glued to the left side of the sample using Loctite® Stycast 2850FT. This resistor was used to create 0.7 s long heat pulses that would initiate the quench.

For NZPV measurements, the critical currents (I_cs) of the samples had to be defined. This was done by measuring the $I-V$ curves of the samples in all temperatures and magnetic fields that would be used in the study. These measurements were continued close to 1 A current, where the PPMS magnetometer's maximum current would be reached. The critical currents were obtained using the 1 $\frac{\mu V}{cm}$ electric field criterion. These critical current values are presented in figure 2. The percentages of the critical currents were calculated from these values. It can be seen that the highest critical currents are in 0 T with the APC-free YBCO. However, the critical currents of the BZO-doped sample in all magnetic field values are higher than or almost equal to the critical currents measured in 1 T for the APC-free YBCO.

NZPV measurements started after the sample had cooled to 70 K within the PPMS. In the measurements, the different current values were applied to the sample one at a time, and for each value the current through the resistor was adjusted accordingly. The resistor current was increased in 1 mA steps until a quench was observed in the voltage values. In figure 3, we have presented a full recovery (a) and a quench that occurred when the resistor current increased 1 mA (b). In full recovery, the thermal energy created by the heat pulse is not sufficient to initiate a quench. This can be seen from the voltage values where the maximum is about 70 mV compared to approximately 100 times higher voltage values in the case of a quench. Because the values are much lower, no part of the sample reaches the normal state and the voltages quickly return to the original values close to 0 V.

Before the heat pulse, the vortices do not move, and the measured voltage is 0 V. During the heat pulse, the thermal energy increases the temperature of the YBCO quickly to temperatures close to T_c, and the TAFF of the vortices begins [28, 29, 38]. This vortex movement creates resistance and heat [28, 29, 34, 38]. The resistance is observed as an increase in the voltage values. Channel 1, which is the channel closest to the heat pulse, reacts strongly to the heat pulse, and some reaction can be clearly seen from the channel 2 voltages as well. However, the system cools too fast for the quench to begin and the voltages return to 0 V. When the quench occurs, the thermal energy heats the YBCO part closest to the resistor so much that the J_c value is reached, and the YBCO begins to change into the normal state [34, 38]. This transition is very sharp after the initial build-up, as can be seen from the changes in the voltage values (see figure 3(b)). After the sharp increase in voltages, the heated part has entered the normal state and the heat is dissipated via electrons to the next part of the microbridge. In full recovery and in overall quench channel 1 starts to react during the heat pulse, but it is not clearly visible in the quench data because of a larger voltage range. The excess thermal energy that is dissipated along the sample decreases along the length of the microbridge. This can be seen from the voltage spike values (see figure 3(b)) that are higher in channels 1 and 2 and decrease so that in channel 4 the voltage values do not spike. This spike results from an increase in the resistance of the normal state YBCO which is caused by the excess thermal energy. After measurements were made for current values that were below 100 mA, the temperature and magnetic field of the system were changed so that in the next measurement the increase in absolute current would be the lowest possible. Using this

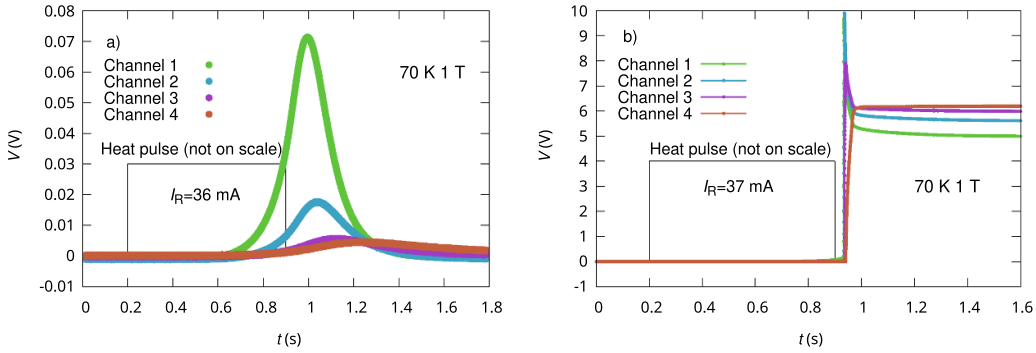

Figure 3. Usual quench development. (a) Full recovery in 70 K 1 T for doped YBCO when the current through the sample was $0.9I_c$ and the current through the resistor was $I_R = 36$ mA. (b) Measured quench in 70 K 1 T for doped YBCO when the current through the sample was $0.9I_c$ and the current through the resistor was $I_R = 37$ mA.

measurement procedure, we tried to avoid breaking the sample as long as possible.

3. Results and discussion

3.1. Differences in APC-free and BZO-doped YBCO films

BZO doping changes the crystallographic structure of YBCO films, while increasing the flux pinning properties [30–34]. These changes affect the values of the critical current density (J_c), which are presented in figure 4. In zero and very low fields, the values of J_c are strongly connected to the coherence length and the penetration depth of the superconductor. Both of these quantities depend on the superconductors electron mean free path [39, 40]. Adding non-superconducting material that works as coherent APCs into the YBCO matrix decreases the mean free path of the electrons. Therefore, the zero field critical current ($J_{c,0}$) is lower in the BZO-doped YBCO [39]. However, the critical current density as a function of the magnetic field decreases greatly for APC-free YBCO. This originates from the fact that there are no strong pinning centers that would counteract the Lorentz force (F_L), which is created by the transport current, that affects the vortices [29]. In BZO-doped YBCO, the decrease in J_c is much more gradual because the formed BZO nanorods, which self-assemble into columnar defects along the *c*-axis of the crystal lattice of YBCO, act as strong pinning centers [31, 33, 34]. The change in the $J_c(B)$ shape is related to the increase in the characteristic accommodation field (B^*) where J_c starts to decrease substantially [33, 41]. B^* is usually defined from the field value where $J_c = 0.9J_{c,0}$ [41]. The increase in B^* can also be seen from the lengthening of the low-field plateau [33, 41]. After reaching the value of B^*, the value of J_c of BZO-doped YBCO also starts to decrease. From figure 4, it can be seen that at some low magnetic field value the $J_c(B)$ curves of the APC-free and BZO-doped YBCO cross, and in larger magnetic field values, the BZO-doped one is able to carry larger currents. This effect can also be seen in figure 2 where almost all critical current values of the BZO-doped sample are higher compared to the I_c values of the APC-free sample in magnetic field. In figure 4 inset, we have shown TEM measurements of APC-free and BZO-doped YBCO, where the formed BZO nanorods

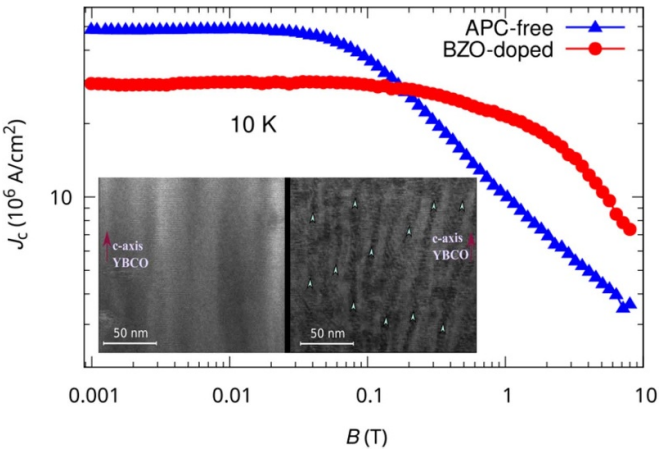

Figure 4. Magnetic field dependencies of the critical current densities of APC-free (blue) and BZO-doped (red) YBCO in 10 K. In the inset, there is a TEM image of both APC-free (left) and BZO-doped (right) YBCO. BZO nanorods are shown with arrows.

can clearly be seen. The average diameter of the nanorods in 4 wt.% BZO-doped YBCO films is ≈6 nm and their average distance from each other is ≈20 nm [40, 42, 43].

3.2. MQE

The idea of MQE is to initiate a quench with the lowest possible thermal energy to minimize the effect of the energy input on the accurate estimation of the NZPV [22]. The MQE was approximated to be MQE $\approx I^2Rt$, where I is the current through the resistor, R is the resistance of the resistor and t is the width of the heat pulse. The resistance did not change much at different temperatures, so 220 Ω value was used in the MQE calculations. The quench measurements for both samples continued until the microbridges broke due to thermal effects caused by the heat pulse and increased current through the sample. For APC-free YBCO this occurred at 30 K 8 T when the current through the sample was $0.9I_c$ and for BZO-doped YBCO it was at 30 K 8 T with $0.5I_c$ current. Due to the different J_c behaviors of the samples, there are more low-temperature points for APC-free YBCO and more 0 T points for BZO-doped YBCO.

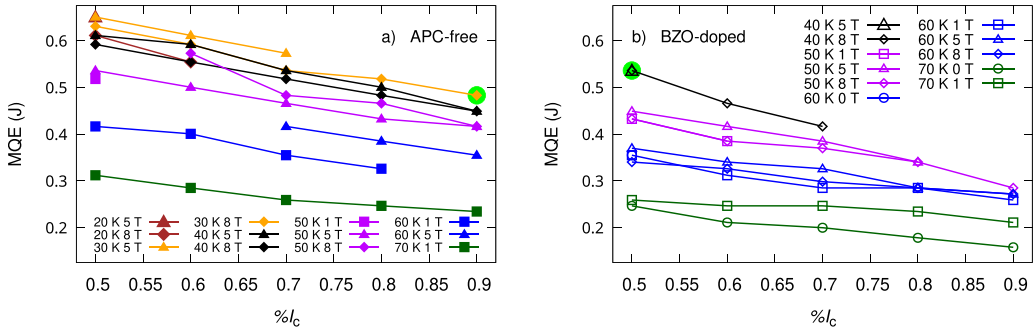

Figure 5. Calculated MQE values for (a) APC-free YBCO and (b) BZO-doped YBCO. The bright green dots indicate the heat pulses that broke both samples at 30 K 8 T. Different temperatures and magnetic fields are indicated by different colors and symbols, respectively.

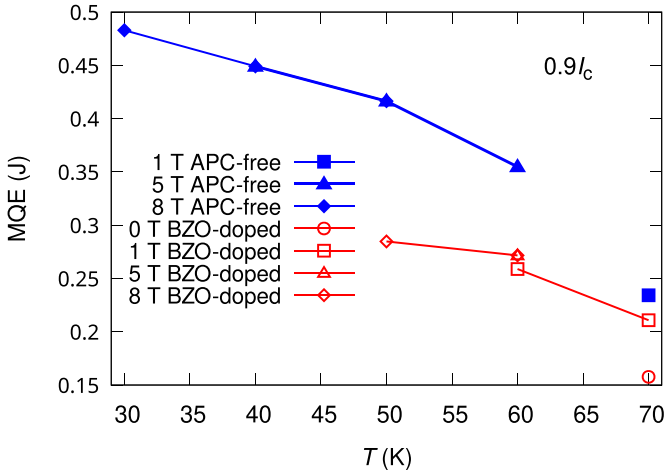

Figure 6. The MQE values when the current through the sample was 0.9I_c. The blue curves correspond to the APC-free sample and the red curves to the BZO-doped sample. Different symbols correspond to different magnetic field values.

In figure 5, the calculated minimum quench energies are presented as a function of the percentage of critical current for both samples. There are also green dots showing the point where the samples broke. It can be seen that the MQE decreases almost linearly as a function of the critical current percentage for both YBCO samples. This indicates that the increase in current, which increases the flux motion through heat and Lorentz force, heats the sample, and less energy is needed from the resistor. The amount of energy required increases with decreasing temperature. At higher temperatures, the vortices have more thermal energy and there are more thermal fluctuations, so the pinning centers have less effect on the vortex motion [28, 29, 38]. Therefore, the heat pulse needs to give less thermal energy to the vortices to start the propagation of the normal zone.

In BZO-doped YBCO, the energies required at the same temperature and field values are smaller than in the APC-free YBCO. From figure 6, where the MQE values are presented as a function of the temperature when the percentage of critical current was kept at 0.9I_c, we can see that at lower temperature the difference between the MQE values is greater. There are points only in 50 K, 60 K, and 70 K that were measured at the same temperature and magnetic field, but the general trend seems to indicate that APC-free YBCO requires more heating power. At lower temperatures, the absolute currents through the BZO-doped sample are larger, and therefore more heat is generated in the initiated normal zone. However, for instance at 70 K 1 T the BZO-doped sample still requires less energy, even though the I_c values are higher in the APC-free sample. Because the differences in the MQE values at 70 K 1 T are quite small, compared to the low-temperature values, it indicates that the absolute current dominates the differences in the MQE values. From the data we can deduce that, at the same temperature and magnetic field, and with approximately the same I_c, the BZO-doped sample requires less energy to initiate a quench. This difference results from the fact that the pinning forces are higher in the BZO-doped sample [31, 39]. Therefore, when the heat pulse transfers thermal energy to the vortices and the temperature starts to increase, the temperature increase in the BZO-doped sample requires less energy. Less energy is required because TAFF is more localized in the BZO-doped sample due to the higher pinning force which reduces the area where heat can dissipate [28, 29, 38]. In the APC-free sample the vortices can move further and the same temperature increase requires more energy from the resistor.

3.3. NZPV

The NZPVs were calculated by taking the time delay between channels 3 and 4 to reach a certain voltage threshold. The distance between the channels is known to be 1 mm. In this work, the threshold was chosen to be 10 mV because it is clearly above the noise level but it is still a low voltage, which indicates the arrival of a normal zone into the channel range. Channels 3 and 4 were chosen because they are the furthest away from the resistor. Ideally, the channels that are the furthest away should be used in order to minimize the over-influence of the original heat pulse on the propagation velocity [9, 13]. In figure 7, we have presented a close up of the quench data of the BZO-doped sample in 40 K 5 T with 0.7I_c current and the 10 mV threshold that was used to calculate the NZPV values.

The calculated NZPVs of both samples are presented in figure 8. In most of the different temperatures and magnetic fields, the NZPV seems to be almost constant for both samples.

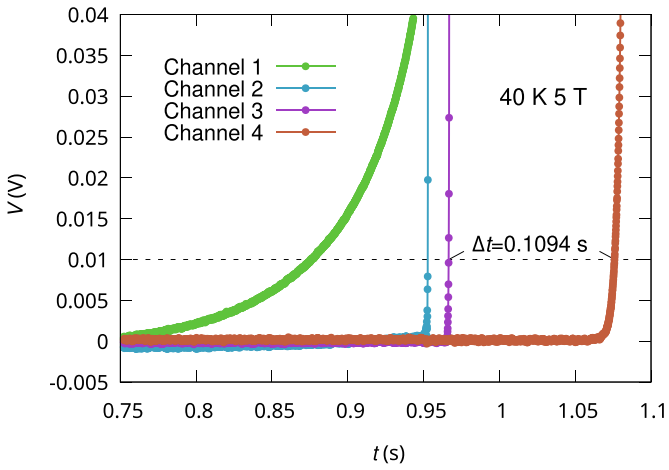

Figure 7. The measured quench data from 40 K 5 T when the current through the sample was $0.7I_c$ for the doped YBCO. The 10 mV threshold used the determine the NZPV values is also shown.

This indicates that the increase in current compensates for the decrease in the heat pulse, thus resulting in a constant movement of the vortices in one specific temperature and magnetic field value. We see that at higher temperature and magnetic field values the NZPV starts to deviate from the constant value. The decrease in NZPV values is only observed at low transport current values ($\leqslant$61 mA) so this could be the reason for the change in the behavior. In lower current values, the driving force created by the Lorentz force decreases [28, 29], and is not compensated by the increase in MQE. Therefore, the decrease in NZPV values results from the transport current becoming so low that it no longer provides enough driving force to move the vortices in the same way as higher transport currents do. In the APC-free sample this effect is more common because the in-field critical current values decrease faster compared to the BZO-doped sample.

The NZPV values seem to generally increase with increasing temperature. This results from the increased thermal energy of the vortices at a higher temperature, which results in a faster heating process. At lower temperature, more energy is also required to heat the sample to normal state, and therefore heating takes more time. In both samples, we can see that generally the magnetic field has a very small effect on the values of NZPV. In the BZO-doped sample, the NZPV values measured at a certain temperature nearly coincide, indicating that the magnetic field has almost negligible effect. In the APC-free sample, different temperature values are closer to each other. This results from the magnetic field dependence of NZPV values, so that the different temperatures start to overlap with each other. These differences arise from larger changes in the I_c values at different magnetic fields. The NZPV values seem to be mostly in the same range of about $10^0\,\frac{\text{mm}}{\text{s}} - 10^2\,\frac{\text{mm}}{\text{s}}$. By comparing the NZPV values of different samples, it can be seen that at higher temperature close to the I_c the normal zone propagates about two times faster in the BZO-doped sample than in the APC-free. At lower temperature the differences start to be smaller until at 40 K the normal zone propagates faster in the APC-free sample. It can also be seen that in the APC-free sample there are more situations where the NZPV changes as a function of $\%I_c$.

3.4. Discussion

According to our study, we found differences in both MQE and NZPV values for YBCO samples with and without APCs. In particular, at lower temperatures the differences in the MQE values were almost double. This difference was found to originate from the different $J_c(B)$-characteristics. These characteristics arise from the enhanced pinning properties of the BZO-doped film resulting in higher transport current values compared to the APC-free film. At higher temperatures, the differences were caused by the pinning strengths of the samples. The differences in the samples resulting in different MQE values are presented in figure 9(a). It was found that the normal zone propagates almost twice as fast in the BZO-doped sample at a higher temperature and close to the critical current. From the MQE values we know that the creation of the normal zone is easier in the BZO-doped sample. As a result, BZO-doped YBCO would be capable of carrying higher current densities and performing more effectively in high magnetic fields, but it would also be more prone to quenching. However, at least at higher operation temperatures and currents, the created normal zone would travel faster and could be detected more easily. This is something that needs to be taken into account when designing high-magnetic-field applications.

NZPVs for coated conductors containing APC-free YBCO have been reported to be in the range of $10^0\,\frac{\text{mm}}{\text{s}} - 10^2\,\frac{\text{mm}}{\text{s}}$ [9, 10, 13, 21–23]. This is quite close to the values that were observed with our two YBCO/STO samples meaning that the behaviour is closer to the classical coated conductors than CFDs that generally have NZPVs in the range of 1–10 $\frac{\text{m}}{\text{s}}$ [24, 26, 27]. Differences arise from NZPV behavior as a function of $\%I_c$. It has been reported that at one temperature and field value the NZPV increases with higher current [9–11, 13, 21, 22]. However, this is something that we do not observe until we reach the low current range and the NZPV starts to decrease with smaller current. These effects are not the same because otherwise we would expect that the NZPV decreases at all different temperature and field values. NZPV has been reported to decrease with higher temperature [9, 10, 21, 23]. This observation is opposite to what we observe in our study. This indicates that the NZPV is more dominated by the operating temperature than by the transport current in YBCO thin films, which is opposite to the behavior in YBCO coated conductors. These differences arise from the different heat propagation mechanisms that occur in YBCO thin films and coated conductors. The mechanisms differ because YBCO thin films lack a stabilizing normal metal layer (Ag and Cu) that would otherwise heat the superconducting sample by Joule heating [13]. As a result, the influence of the transport current on normal zone propagation is less significant. The effect of the substrates is negligible, since both STO and the buffer layers on top of the Hastelloy are insulators and no current will flow in them [11]. The differences between YBCO thin films grown on STO substrates and, on the other hand, YBCO coated conductors are presented in figure 9(b).

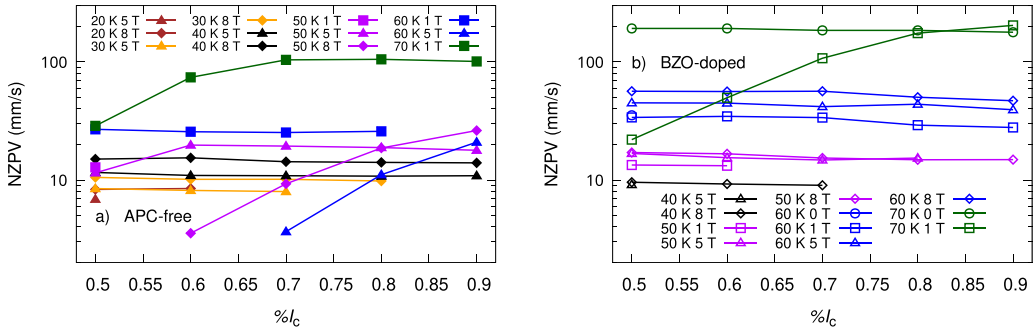

Figure 8. Calculated NZPV values for (a) APC-free YBCO and (b) BZO-doped YBCO. Different temperatures and magnetic fields are indicated by different colors and symbols, respectively.

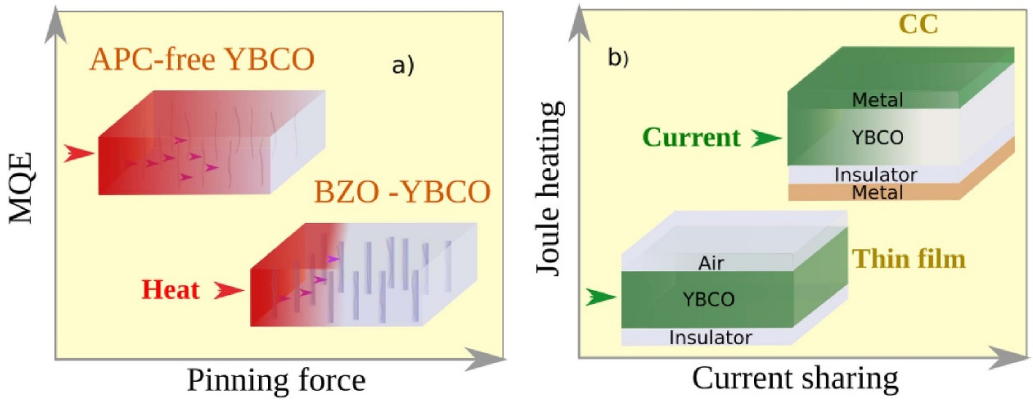

Figure 9. Schematic illustrations of (a) heat dissipation differences between APC-free and BZO-doped YBCO films, and on the other hand, (b) current flow differences between YBCO grown on insulating single crystal STO substrate and YBCO coated conductor. The YBCO coated conductor generally consists of YBCO grown on a Hastelloy substrate that has insulating buffer layers between the metal and YBCO. This structure is then capped by a thin protective silver layer and surrounded by copper [13]. In (a), because the pinning force is greater in the BZO-doped YBCO, the heat dissipation is reduced to a smaller area and results in a faster temperature increase. In (b), when the temperature of the YBCO starts to increase in a coated conductor, the current starts to flow in the stabilizing metal layers instead of YBCO. In YBCO thin films grown on STO, there are no layers where the current can flow except the YBCO.

MQE values for coated conductors have been reported to be in the range of $10^{-1} - 10^{1}$ J [9, 10, 21, 23]. Our measurements are in this range but on the lower side. It has also been observed that MQE decreases with higher temperature [9, 21, 23] as well as with higher current [9, 10, 21, 23]. Both observations are in line with our measurements, indicating that MQE behavior is less influenced by Joule heating from the normal metal layer than the NZPV behavior. This is reasonable to expect, because the initial stage of the quench is primarily governed by the temperature rise in YBCO. At first, the normal metal layer just increases the thermal mass of the system, which means that more energy is required to increase the temperature [24]. This is seen as higher MQE values.

4. Conclusions

In this work, we studied the differences in the quench characteristics between APC-free YBCO and BZO-doped YBCO. Our studies revealed that the NZPV values did not have large differences, but the MQEs required to quench the samples were lower in the BZO-doped sample. This difference was concluded to originate from the different flux pinning properties of the samples.

In comparison of our results with those of the literature, we noted that the NZPV behavior was different compared to the YBCO coated conductors. It was realized that the heat dissipation mechanisms that dominate the propagation of the normal zone are different in our samples compared to coated conductors. This was explained by the lack of conductive metal layer in contact with YBCO. This work provided deeper insight into the quench characteristics of YBCO, despite coated conductors being primarily used in practical applications.

Data availability statement

All data that support the findings of this study are included within the article (and any supplementary files).

Acknowledgment

The Jenny and Antti Wihuri Foundation is acknowledged for financial support.

ORCID iDs

S Mejia 0009-0000-5245-8230
M M Aye 0000-0001-8021-118X
H Huhtinen 0000-0002-2166-5939
P Paturi 0000-0002-6240-2801

References

[1] Miller J 2003 *IEEE Trans. Appl. Supercond.* **13** 1385–90
[2] Bergen A *et al* 2019 *Supercond. Sci. Technol.* **32** 125006
[3] Labbé A, Authelet G, Baudouy B, van der Beek C J, Briatico J, Darrasse L and Poirier-Quinot M 2021 *Front. Phys.* **9** 705438
[4] Ball P 2021 *Nature* **599** 362–6
[5] Molodyk A *et al* 2021 *Sci. Rep.* **11** 2084
[6] Parizh M, Lvovsky Y and Sumption M 2017 *Supercond. Sci. Technol.* **30** 1–16
[7] Wang X, Gourlay S A and Prestemon S O 2019 *Instruments* **3** 1–27
[8] Mitchell N *et al* 2021 *Supercond. Sci. Technol.* **34** 1–57
[9] Wang X, Trociewitz U P and Schwartz J 2007 *J. Appl. Phys.* **101** 053904
[10] van Nugteren J, Dhalle M, Wessel S, Krooshoop E, Nijhuis A and ten Kate H 2015 *Phys. Proc.* **67** 945–51
[11] Giguere J, Lacroix C, Dupuis-Desloges F, Fournier-Lupien J H and Sirois F 2021 *Supercond. Sci. Technol.* **34** 045010
[12] Marchevsky M 2021 *Instruments* **5** 27
[13] Iannone G, D'Agostino D, Saggese A, Celentano G and Gambardella U 2020 *Cryogenics* **109** 103116
[14] Iwasa Y 2003 *Cryogenics* **43** 303–16
[15] Chiuchiolo A, Palmieri L, Consales M, Giordano M, Borriello A, Bajas H, Galtarossa A, Bajko M and Cusano A 2015 *Opt. Lett.* **40** 4424–7
[16] Huang X, Gonzales J T and Badcock R A 2023 *Measurement* **214** 112796
[17] Lee H, Kim H M, Jankowski J and Iwasa Y 2004 *IEEE Trans. Appl. Supercond.* **14** 1298–301
[18] Marchevsky M and Gourlay S A 2017 *Appl. Phys. Lett.* **110** 012601
[19] Hasegawa S, Ito S, Nishijima G and Hashizume H 2021 *IEEE Trans. Appl. Supercond.* **31** 1–5
[20] Bykovskiy N, Uglietti D, Bruzzone P and Sedlak K 2022 *IEEE Trans. Appl. Supercond.* **32** 1–5
[21] Wang X, Caruso A, Breschi M, Zhang G, Trociewitz U, Weijers H and Schwartz J 2005 *IEEE Trans. Appl. Supercond.* **15** 2586–9
[22] Zhong Z, Ruiz H S, Lai L, Huang Z, Wang W and Coombs T 2015 *IEEE Trans. Appl. Supercond.* **25** 1–5
[23] Park H, Kim A, Park M, Yu I, Eom B, Bae J, Kim S, Sim K and Sohn M 2010 *IEEE Trans. Appl. Supercond.* **20** 2122–5
[24] Lacroix C *et al* 2022 *Supercond. Sci. Technol.* **35** 1–9
[25] Lacroix C and Sirois F 2014 *Supercond. Sci. Technol.* **27** 035003
[26] Barusco P, Ben-Saad H, Horn-Bourque D, Lacroix C, Sirois F, Puig T, Gutiérrez J, Granados X and Obradors X 2024 *IEEE Trans. Appl. Supercond.* **34** 1–6
[27] Ben Saad H, Lacroix C, Zhuldybina M and Sirois F 2024 *Supercond. Sci. Technol.* **37** 125019
[28] Nikolo M 1993 *Supercond. Sci. Technol.* **6** 618
[29] Blatter G, Feigel'man M V, Geshkenbein V B, Larkin A I and Vinokur V M 1994 *Rev. Mod. Phys.* **66** 1125–388
[30] Peurla M, Paturi P, Stepanov Y P, Huhtinen H, Tse Y Y, Bódi A C, Raittila J and Laiho R 2006 *Supercond. Sci. Technol.* **19** 767–71
[31] Emergo R L S, Baca F J, Wu J Z, Haugan T J and Barnes P N 2010 *Supercond. Sci. Technol.* **23** 115010
[32] Song K J *et al* 2006 *Physica C* **445–448** 656
[33] Huhtinen H, Peurla M, Shakhov M A, Stepanov Y P, Paturi P, Raittila J, Palai R and Laiho R 2007 *IEEE Trans. Appl. Supercond.* **17** 3620
[34] Sadovskyy I A *et al* 2016 *Adv. Mater.* **28** 4593–600
[35] Aye M M *et al* 2021 *Sci. Rep.* **11** 1–11
[36] Khan M Z, Rivasto E, Rijckaert H, Zhao Y, Liedke M O, Butterling M, Wagner A, Van Driessche I, Huhtinen H and Paturi P 2022 *Cryst. Growth Des.* **22** 2097–104
[37] Wiesinger H P, Sauerzopf F M and Weber H W 1992 *Physica C* **203** 121–8
[38] Poole J C P, Farach H A Creswick R J and Prozorov R 2007 *Superconductivity* 2nd edn (Academic)
[39] Paturi P and Huhtinen H 2022 *Supercond. Sci. Technol.* **35** 1–9
[40] Aye M M, Rivasto E, Khan M Z, Rijckaert H, Palonen H, Huhtinen H, Van Driessche I and Paturi P 2021 *New J. Phys.* **23** 1–12
[41] Klaassen F C, Doornbos G, Huijbregtse J M, van der Geest R C F, Dam B and Griessen R 2001 *Phys. Rev. B* **64** 1–20
[42] Aye M M, Rivasto E, Rijckaert H, Palonen H, Huhtinen H, Van Driessche I and Paturi P 2022 *Supercond. Sci. Technol.* **35** 1–10
[43] Aye M M, Rivasto E, Huhtinen H and Paturi P 2024 *Cryst. Growth Des.* **24** 4545–55